

A complete analysis of the laser beam deflection systems used in cantilever-based systems

L.Y. Beaulieu^{a,*}, Michel Godin^b, Olivier Laroche^c, Vincent Tabard-Cossa^c, Peter Grütter^c

^a*Department of Physics and Physical Oceanography, Memorial University, St. John's, NL., Canada A1B 3X7*

^b*Division of Biological Engineering, Media Laboratory, Massachusetts Institute of Technology, 20 Ames Street, Cambridge, MA 02139, USA*

^c*Physics Department, McGill University, Montreal, QC., Canada H3A 2T8*

Received 20 February 2006; received in revised form 2 November 2006; accepted 2 November 2006

Abstract

A working model has been developed which can be used to significantly increase the accuracy of cantilever deflection measurements using optical beam techniques (used in cantilever-based sensors and atomic force microscopes), while simultaneously simplifying their use. By using elementary geometric optics and standard vector analysis it is possible, without any fitted or adjustable parameters, to completely and accurately describe the relationship between the cantilever deflection and the signal measured by a position sensitive photo-detector. By arranging the geometry of the cantilever/optical beam, it is possible to tailor the detection system to make it more sensitive at different stages of the cantilever deflection or to simply linearize the relationship between the cantilever deflection and the measured detector signal. Supporting material and software has been made available for download at http://www.physics.mun.ca/beaulieu_lab/papers/cantilever_analysis.htm so that the reader may take full advantage of the model presented herein with minimal effort.

© 2006 Elsevier B.V. All rights reserved.

Keywords: Cantilever; Optical beam deflection; Cantilever sensor; AFM

1. Introduction

Micro-cantilevers are small V-shaped or rectangular cantilevers (typically made of silicon nitride (SiN_x) or silicon (Si)) which are of the order of 400 μm long, 50 μm wide and 1 μm thick. Although micro-cantilevers are typically used in atomic force microscopes (AFM) for surface imaging, they have also been employed as ultra-sensitive sensors to detect various phenomena such as changes in temperature [1], changes in mass [2] and the detection of chemical reactions through changes in surface stress [3].

Properly measuring the cantilever deflection is at the heart of acquiring precision measurements when performing cantilever-based sensing or atomic force spectroscopy experiments. The most common method to measure the cantilever deflection is by using an optical beam deflection

system [4]. Although there have been some discussions in the literature regarding the laser detection scheme [5–15], we have not seen addressed anywhere the subject of how to obtain a well-defined relationship between the actual cantilever deflection and the PSD signal. Nor have we seen anywhere discussed the influence of different optical beam deflection geometries on the relationship between the cantilever deflection and the PSD signal. This is the subject of this paper.

In a recent paper, we have reported how, by properly designing a cantilever-based instrument, it is possible to linearize the relationship between the cantilever deflection and the measurement made with a photo-sensitive detector (PSD) [16]. In this paper, we describe in full detail the mathematical model used to properly characterize the cantilever/laser beam deflection system so that potential users may adapt and use the model with their instruments. We also provide a web link where the reader can download software and other supporting material related to this paper.

*Corresponding author. Tel.: +1 709 7376203; fax: +1 709 7378739.
E-mail address: beaulieu@physics.mun.ca (L.Y. Beaulieu).

2. Theory

Fig. 1 shows a schematic representation that describes the geometry of a cantilever/laser beam detection system. In this diagram, the cantilever surface is in the x – y plane and is oriented in the positive x direction. The cantilever chip is fixed in space and does not move. An incident laser hits the cantilever at a distance D from the base of the cantilever chip. The incident laser is fixed at an angle of inclination θ with respect to the x – y plane and at an azimuthal angle ϕ measured from the positive x -axis. The laser reflects off the free end of the cantilever into a position sensitive detector (PSD) held at an initial distance L from the cantilever. The PSD is itself inclined at an angle ξ also with respect to the x – y plane. In Fig. 1, the line labeled \mathbf{N}_c , is the vector normal to the surface of the cantilever and is used to calculate the reflected laser beam direction in accordance with the law of reflection.

The vector equation for a straight line in three dimensions is given by

$$\mathbf{I} = \mathbf{I}_p + t\mathbf{I}_a, \quad (1)$$

where \mathbf{I}_p is any point on the line, \mathbf{I}_a is the unit direction vector and t is any scalar. In this case \mathbf{I}_p is defined as the initial point where the incident laser hits the cantilever at $\mathbf{I}_p = (D, 0, 0)$. Given the geometry shown in Fig. 1, the direction vector \mathbf{I}_a is defined as

$$\mathbf{I}_a = (\cos(\theta) \cos(\pi - \phi), \cos(\theta) \sin(\pi - \phi), -\sin(\theta)). \quad (2)$$

During cantilever deflections, the incident laser beam reflects away from the surface normal in accordance to the law of reflection. Therefore it is imperative that the proper cantilever curvature be taken into consideration. In cantilever sensor experiments, it has been reported that the cantilever undergoes a deflection as if it were subjected to an end-moment [17,18]. For this type of deflection the curvature of the cantilever is described by the following equation:

$$z(x) = \gamma x^2. \quad (3)$$

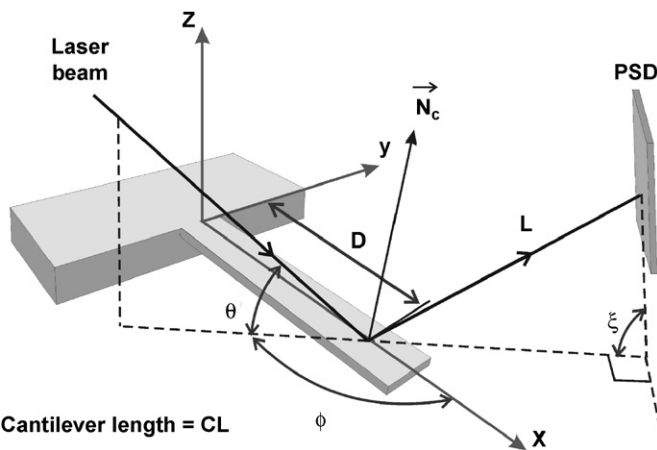


Fig. 1. Schematic representation of a laser reflecting from a cantilever into a PSD detector.

In this equation, γ is a constant defined by the physical parameters of the cantilever multiplied by the applied end moment force. In the following calculations, the end deflection of the cantilever is controlled which in turn governs the value of γ . Therefore, at each calculated deflection, γ is defined as

$$\gamma = \frac{z(x_{\max})}{x_{\max}^2}. \quad (4)$$

The value of x_{\max} is determined by solving the integral equation, which defines the total length CL of the cantilever.

$$\begin{aligned} CL &= \int_0^{x_{\max}} \sqrt{\left(1 + \left(\frac{\partial z}{\partial x}\right)^2\right)} dx \\ &= \int_0^{x_{\max}} \sqrt{\left(1 + \left(2\frac{z(x_{\max})}{x_{\max}^2}x\right)^2\right)} dx \\ &= \frac{2z(x_{\max})\sqrt{x_{\max}^2 + 4z(x_{\max})^2} - x_{\max}^2 \ln(x_{\max})}{4z(x_{\max})} \\ &\quad + \frac{x_{\max}^2 \ln(2z(x_{\max}) + \sqrt{x_{\max}^2 + 4z(x_{\max})^2})}{4z(x_{\max})} \end{aligned} \quad (5)$$

Solving for x_{\max} from Eq. (5) is done numerically.

During AFM force spectroscopy experiments, a point load is applied to the end of the lever. Such a force causes a cantilever to deflect with a curvature as described by Eq. (6) [19]

$$z(x) = \frac{Fx^2}{6EI}(x - 3a), \quad (6)$$

where F is the applied force, E is the Young's Modulus of elasticity, I is the area moment of inertia, and a is the location of the applied force. As before, in order to perform the simulations, the cantilever curvature needs only to be described using Eq. (7).

$$z(x) = \gamma x^2(x - 3a), \quad (7)$$

where γ is determined by the maximum deflection.

$$\gamma = \frac{z(x_{\max})}{x_{\max}^3 - 3ax_{\max}^2}. \quad (8)$$

The value of x_{\max} is determined by solving the length equation

$$\begin{aligned} CL &= \int_0^{x_{\max}} \sqrt{\left(1 + \left(\frac{\partial z}{\partial x}\right)^2\right)} dx \\ &= \int_0^{x_{\max}} \sqrt{\left(1 + (\gamma(3x^2 - 6ax))^2\right)} dx \end{aligned} \quad (9)$$

the solution of which is too lengthy to show here. Solving this equation numerically gives the coordinate of the end of the lever (x_{\max} , z_{end}).

When the cantilever deflects, the intersection point \mathbf{W} between the incident laser and the cantilever surface must be calculated. This is accomplished by solving the

vector equation

$$\mathbf{I} = \mathbf{I}_p + t\mathbf{I}_a = (W_x, W_y, \gamma W_x^2) = \mathbf{W}$$

(End moment deflection),

$$\mathbf{I} = \mathbf{I}_p + t\mathbf{I}_a = (W_x, W_y, \gamma W_x^2(W_x - 3a)) = \mathbf{W}$$

(Point load deflection). (10)

At the contact point \mathbf{W} between the incident laser and the cantilever, it is necessary to obtain the vector normal \mathbf{N}_c to the cantilever surface. The slope m_{N_c} of the vector \mathbf{N}_c is given by the negative of the reciprocal of the slope of the cantilever at the point \mathbf{W} . This can be written as

$$m_{N_c} = -\frac{1}{2\gamma W_x} \quad (\text{End moment deflection}), \quad (11)$$

$$m_{N_c} = -\frac{1}{\gamma(3W_x^2 - 6aW_x)} \quad (\text{Point load deflection}). \quad (12)$$

Defining the angle $\varepsilon = \arctan(m_{N_c})$, the vector \mathbf{N}_c may be written as

$$\mathbf{N}_c = (\cos(\varepsilon), 0, \sin(\varepsilon)). \quad (13)$$

The direction vector of the reflected beam \mathbf{R}_a is by definition, the reflection of \mathbf{I}_a across \mathbf{N}_c in the \mathbf{I}_a – \mathbf{N}_c plane. This is a well-known formula [20] given by Eq. (14).

$$\mathbf{R}_a = \mathbf{I}_a - (2\mathbf{I}_a \cdot \mathbf{N}_c)\mathbf{N}_c. \quad (14)$$

As in the case of the incident beam, the vector line of the reflected beam \mathbf{R} is given by the vector equation

$$\mathbf{R} = \mathbf{W} + t\mathbf{R}_a. \quad (15)$$

As one of the adjustable parameters, the PSD/cantilever separation is given by the value L . The value of L is used to define the initial contact point \mathbf{PSD}_p of the reflected laser on the PSD

$$\mathbf{PSD}_p = \mathbf{I}_p + L\mathbf{R}_a. \quad (16)$$

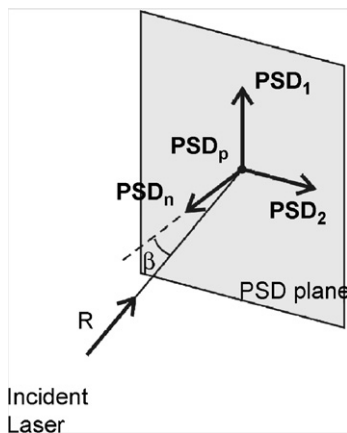


Fig. 2. Schematic representation of the vector geometry involved in characterizing the plane of the PSD. The vector \mathbf{PSD}_n is normal to the PSD plane while the vectors \mathbf{PSD}_1 and \mathbf{PSD}_2 are in the PSD plane. In this diagram, the vector \mathbf{R} represents the reflected laser beam, which is incident on the PSD at the point \mathbf{PSD}_p . The vector \mathbf{R} subtends an angle β with respect to the PSD surface normal.

Table 1

For $\phi = 0^\circ$	$\mathbf{PSD}_1 = (\cos(\xi), 0, \sin(\xi)),$ $\mathbf{PSD}_2 = (0, 1, 0)$	(17)
----------------------	---	------

For $\phi = 90^\circ$	$\mathbf{PSD}_1 = (0, -\cos(\xi), \sin(\xi)),$ $\mathbf{PSD}_2 = (1, 0, 0)$	(18)
-----------------------	--	------

For $\phi = 180^\circ$	$\mathbf{PSD}_1 = (-\cos(\xi), 0, \sin(\xi)),$ $\mathbf{PSD}_2 = (0, -1, 0)$	(19)
------------------------	---	------

The vector \mathbf{PSD}_p is determined at the beginning of the algorithm and remains fixed for the duration of the calculations. The active area of the PSD is described as a plane in space. Describing such a plane requires a point \mathbf{PSD}_p and a normal vector \mathbf{PSD}_n (see Fig. 2). The normal vector \mathbf{PSD}_n is determined by two orthogonal vectors defined by the geometry in Fig. 1. Fig. 2 shows a schematic representation of the geometry used to describe the PSD. In this diagram, the vector \mathbf{PSD}_n is normal to the PSD plane while the vectors \mathbf{PSD}_1 and \mathbf{PSD}_2 are in the PSD plane. Also, since the PSD plane is inclined with respect to the x – y plane, the vector \mathbf{PSD}_n may not necessarily be parallel to the reflected laser beam vector \mathbf{R} . In all calculations, the vectors \mathbf{I} , \mathbf{R} , and \mathbf{PSD}_n all lie in the same plane. The vectors describing the PSD plane are shown in Table 1 for three specific cases.

Finally, the vector normal to the PSD plane is given by the following vector product:

$$\mathbf{PSD}_n = \mathbf{PSD}_2 \times \mathbf{PSD}_1. \quad (20)$$

Once the PSD plane has been defined, it is then necessary to determine the intersection point \mathbf{rPSD} between the PSD plane and the reflected laser \mathbf{R} . This is done by using the following equation [20]:

$$\mathbf{rPSD} = \mathbf{W} + \frac{(\mathbf{PSD}_p - \mathbf{W}) \cdot \mathbf{PSD}_n}{\mathbf{R}_a \cdot \mathbf{PSD}_n} \mathbf{R}_a. \quad (21)$$

The algorithm described above is performed for a range of cantilever deflections (i.e. from 0 to some end deflection). Since the PSD plane is inclined in 3D space, it is necessary to rotate it such as to transform it into 2D space. This is shown schematically in Fig. 3.

The general rotation matrix \mathbf{M} used to rotate any vector by an angle β about a vector \mathbf{u} is given by the following [20]:

$$\mathbf{M} = \begin{bmatrix} u_x^2 + C(1 - u_x^2) & u_x u_y(1 - C) - u_z S & u_x u_z(1 - C) + u_y S \\ u_x u_y(1 - C) + u_z S & u_y^2 + C(1 - u_y^2) & u_y u_z(1 - C) - u_x S \\ u_x u_z(1 - C) - u_y S & u_y u_z(1 - C) + u_x S & u_z^2 + C(1 - u_z^2) \end{bmatrix}, \quad (22)$$

where $C \equiv \cos(\beta)$ and $S \equiv \sin(\beta)$.

Although $\beta = \pi/2 - \xi$, the value of \mathbf{u} changes depending on which system is being studied. Table 2 shows the different values of \mathbf{u} .

Throughout this paper the linearity of the PSD measurement versus cantilever deflection curves is discussed.

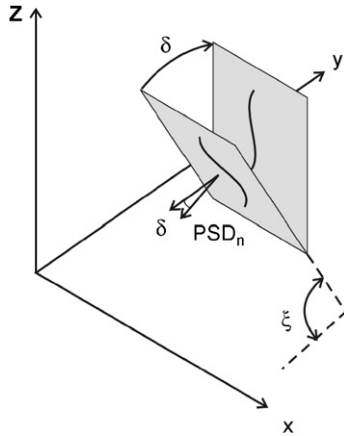


Fig. 3. Schematic representation showing how the PSD plane in 3D is rotated by an angle $\delta = \pi/2 - \zeta$ into a 2D plane.

Table 2

System	Value of ϕ	Vector \mathbf{u}
1	$\phi = 0^\circ$	$\mathbf{u} = (0, -1, 0)$
2	$\phi = 90^\circ$	$\mathbf{u} = (-1, 0, 0)$
3	$\phi = 180^\circ$	$\mathbf{u} = (0, 1, 0)$

In order to compare the linearity of different data we will quote the value of χ^2 given by the following:

$$\chi^2 = \sum_n (r\text{PSD}(z_n(x_{\max})) - mz_n(x_{\max}))^2, \quad (23)$$

where $r\text{PSD}(z_n(x_{\max}))$ is the calculated PSD measurement for a specific cantilever deflection $z_n(x_{\max})$ at the end point of the cantilever x_{\max} and m is the slope of the best fit line.

3. Equipment

Matching experiments performed to validate the above model were conducted on a macro-sized cantilever made in-house. The rectangular-shaped cantilever was constructed from a 3.17 mm thick aluminum piece, 25.4 mm wide with an extended unsupported length of 410 mm. The cantilever was held horizontally approximately 2 mm from a solid aluminum plate in which holes capable of accepting dowel pins were machined at precise locations such as to force the cantilever to bend with the desired curvature as required by different bending mechanisms. A standard undergraduate laboratory HeNe laser was used to monitor the deflection of the cantilever. In order to promote the reflection of the laser off the cantilever surface, the free end of the lever was machined polished to a mirror finish. The large size of this system made the measurement of each parameter D , L , CL , ϕ , θ , and ζ possible with high precision.

4. Results

Fig. 4 shows experimental (symbols) and calculated data (solid lines) of the PSD displacement versus cantilever deflection for system 3 described in Table 2. The PSD signal is given in units of length which describes the displacement of the incident laser spot on the PSD. Most cantilever-based instruments use a PSD where a measured voltage is linearly proportional to the displacement of the laser on the PSD. Hence the PSD displacement versus cantilever deflection data as shown here is consistent with current technology. The two plots 4 (a) and (b) show data taken where the values of D , L , ϕ and θ are fixed and ζ varies from 0° to 90° . As the data shows, excellent agreement is obtained between the experimental and calculated data. It is important to stress that the above model completely and accurately describes the measured data *without the use of any adjustable or fitted parameters*. The values of D , L , CL , ϕ , θ , and ζ uniquely defines the cantilever/laser beam detection system. Fig. 4 shows how the concavity of the data changes as the value of ζ is changed (similar results occur if D , L , ϕ and ζ are fixed and θ is varied). The PSD versus cantilever deflection curve goes from concave to convex as the PSD angle is changed from 0.0° to 90.0° , respectively. The change in curvature can easily be rationalized when the geometry of the reflected laser and the angle of the PSD are taken into consideration. As the PSD/Cantilever deflection curve goes

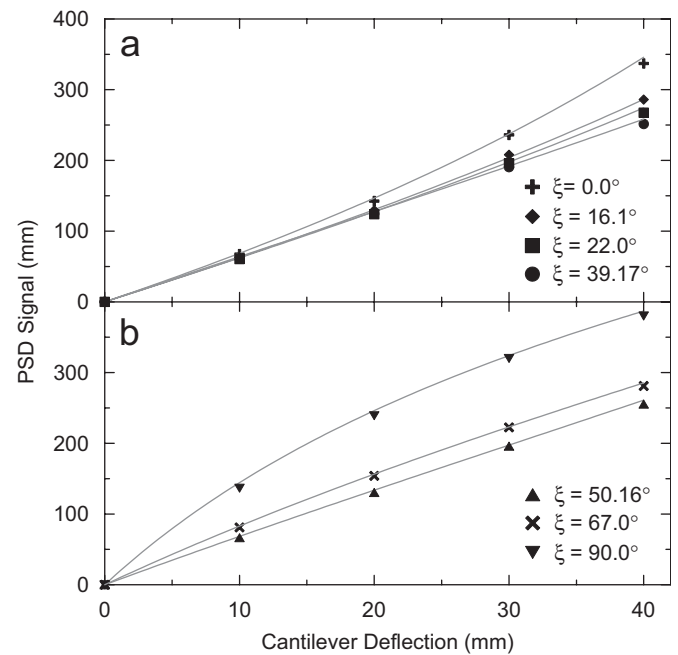


Fig. 4. Comparison between experimental (symbols) and calculated data (solid lines) for the PSD displacement versus cantilever deflection of system 3 described in Table 2 for different values of PSD angle (a) $\zeta = 0.0^\circ, 16.1^\circ, 22.0^\circ, 39.17^\circ$ and (b) $\zeta = 50.16^\circ, 67.0^\circ, 90.0^\circ$. The macro-cantilever was forced to deflect by an end-moment. The fixed geometrical parameters of the system were: $D = 382.5 \pm 0.5$ mm, $L = 603.7 \pm 0.5$ mm, $CL = 410.0 \pm 0.5$ mm, $\phi = 180.0 \pm 0.5^\circ$, $\theta = 69.9 \pm 0.5^\circ$.

from concave to convex, it passes a region where the relationship is nearly linear. We have found that for any geometry D , L , CL , ϕ , θ , and bending curvature, it is possible to find a PSD angle ζ (or ζ fixed and θ is varied) such that the linearity of the relationship between the PSD and the cantilever deflection is maximized.

As an example, the geometry: $CL = 375 \mu\text{m}$, $D = 350 \mu\text{m}$, $L = 3.0 \text{ cm}$, $\phi = 180^\circ$ (system 3), and $\theta = 70^\circ$ is characteristic of a typical cantilever sensor setup used in our laboratory. For this geometry, assuming a maximum cantilever deflection of $40 \mu\text{m}$, it can be found by least-squares-fit that the optimized PSD angle is $\zeta = 37.25^\circ$. Fig. 5a shows a comparison between calculated data (gray crosses) and a linear fit (solid line) showing the linearity of the PSD signal. Fig. 5b shows, on a much-reduced scale, the difference between the optimized linear PSD/cantilever curve and the straight line fit. At most, a difference of 40 nm corresponds, as shown in Fig. 5c to an error of 0.08% of the maximum PSD measurement. In fact, calculations have shown that regardless of the values of D , L , ϕ , and θ , it is always possible to find a value of ζ that maximizes the linearity of the relationship between the PSD signal and the cantilever deflection.

When attempting to linearize the PSD versus cantilever deflection relationship, it is important to note that not only does the value of ζ depend on the parameters D , L , CL , ϕ , and θ , but it also depends on the maximum cantilever deflection (range). Fig. 6a) shows how the optimized PSD angle ζ varies with the maximum cantilever deflection. The reason for this dependence stems from the fact that the relationship between the PSD displacement and the cantilever deflection is not perfectly linear as shown in Fig. 5b. The PSD displacement/cantilever deflection curve oscillates, although minutely, about the best-fit line used to obtain the PSD angle ζ . Therefore, depending on the deflection range used in the analysis, the value of ζ will differ. However the data shows that the value of ζ becomes stationary for small cantilever deflections ($< 3 \mu\text{m}$) which is the range where most cantilever-based experiments occur. Fig. 6b reveals that χ^2 also decreases as the cantilever deflection range decreases. This indicates that the accuracy of the fit increases when smaller cantilever deflections are considered. However, even for large deflections, the linearity of the optimized geometry is still adequate as shown by the small value of χ^2 .

As the cantilever deflects, the position where the laser beam hits the cantilever also changes. As expected for system 3 (Table 2), the x -position (see Fig. 1) of the intersection point of the incident laser beam on the cantilever (the x -coordinate of the vector \mathbf{W}) increases with cantilever deflection. Our model can be used to completely describe the position of the laser spot on the cantilever for any deflection. Fig. 7 shows a plot of the displacement of the intersection point between the incident laser beam and the cantilever as measured directly along the length of the lever versus cantilever deflection. The graph shows a comparison between measured data (black

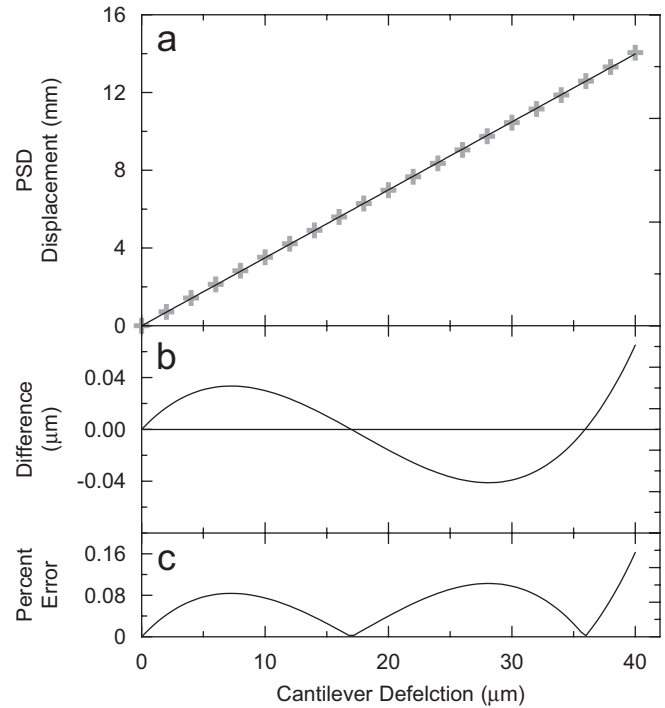


Fig. 5. (a) Calculated data (gray crosses) and linear fit (solid line) for an optimized setup with $CL = 375 \mu\text{m}$, $D = 350 \mu\text{m}$, $L = 3.0 \text{ cm}$, $\phi = 180^\circ$, $\theta = 70^\circ$ and $\zeta = 37.25^\circ$. (b) Difference between the calculated data and best line of fit. (c) Percent error of the linearity fit.

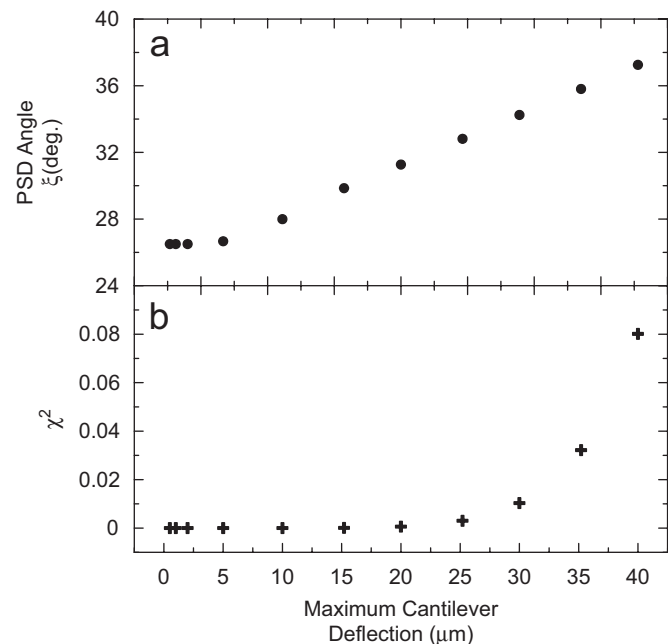


Fig. 6. (a) Calculated results showing how for the following geometry, $CL = 375 \mu\text{m}$, $D = 350 \mu\text{m}$, $L = 3.0 \text{ cm}$, $\phi = 180^\circ$, $\theta = 70^\circ$, the optimized angle of the PSD changes with the maximum cantilever deflection. (b) Calculated results showing how χ^2 increases when the maximum cantilever deflection increases. This result indicates that the relationship between the PSD signal and the cantilever deflection for an optimized geometry becomes increasing linear when small maximum cantilever deflections are considered.

circles) as taken with the macro-cantilever and the results of the model (solid gray line). Clearly the model completely and accurately describes the position of the laser spot on the cantilever. Again it is important to emphasize that no adjustable parameters are used anywhere in this analysis. For the case of a laser reflecting off a cantilever in a typical AFM, an end deflection of 10 μm would cause the incident laser to undergo a total displacement of approximately 3 μm on the cantilever surface.

Although system 3 (Table 2) is the most commonly used geometry for cantilever-based instruments, there are other geometries that can be used to monitor the cantilever deflection. Fig. 8 shows experimental data (symbols) taken with the macro-cantilever and calculated curves from the model of the PSD signal versus cantilever deflection for the following geometries: $\phi = 0^\circ$, $\theta = 69.9^\circ$, $L = 603.7 \text{ mm}$, $D = 383.5 \text{ mm}$, $\text{CL} = 410 \text{ mm}$ and $\xi = 9.55^\circ$, 39.75° , and 59.64° . As in the previous case the model perfectly describes the $\phi = 0^\circ$ system. The main difference between systems 1 and 3 is in the relationship between the incident laser beam \mathbf{I} and the normal vector \mathbf{N}_c . In the case of system 3, the angle between \mathbf{I} and \mathbf{N}_c continuously increases while for system 1 the angle continuously decreases during cantilever deflections. As a consequence, system 1 imposes more physical restrictions for it requires that the PSD and the laser focusers be in close proximity to each other since the angle of incidence (and reflection) becomes smaller as the cantilever bends. A second consequence imposed by physical restriction is that it is more difficult to obtain a strongly convex relationship between the PSD signal and the cantilever deflection then for system 3. However the opposite is true for producing a concave relationship.

As in the case for $\phi = 180^\circ$, it is possible to linearize the relationship between the PSD displacement and cantilever deflection for system 1 ($\phi = 0^\circ$) by optimizing the PSD angle ξ (or incident laser angle θ). Fig. 9 shows calculated

data for $\phi = 0^\circ$, $\theta = 70^\circ$, $L = 3 \text{ cm}$, $D = 325 \mu\text{m}$, $\text{CL} = 350 \mu\text{m}$ and an optimized PSD angle of $\xi = 13.89^\circ$. These values are typical dimensions for actual cantilever sensors. Fig. 9a shows the calculated PSD displacement (gray symbols) versus cantilever deflection for the optimized geometry along with a linear best-fit line (solid line). The difference between these two curves is shown on a reduced scale in Fig. 9b and the relative percent error in Fig. 9c. With a $\chi^2 = 0.04$, these values are comparable to those found for the $\phi = 180^\circ$ system and represent an uncertainty well within experimental noise.

Also similar to the $\phi = 180^\circ$ system, it is possible to model the motion of the laser spot on the cantilever as the cantilever is forced to deflect. For this case however, as the cantilever deflects the laser spot moves up the length of the cantilever (closer to the chip). As in the previous case, excellent agreement was obtained between experimental and calculated values.

Both systems 1 and 3 (Table 2) are very similar and differ only by their geometry. Specifically both show similar behavior and accuracy regardless of the types of cantilever deflections used. However, system 2 characterized by $\phi = 90^\circ$ (see Fig. 1) is very different than systems 1 and 3 ($\phi = 0^\circ$ and 180° , respectively) where the length of the cantilever, the incident and reflected laser are all restricted to the x - z plane. For the case of $\phi = 90^\circ$, the incident laser is parallel to the y - z plane. Because of this, the PSD signal is no longer a straight line but a curve as shown schematically in Fig. 10. Notice that for the $\phi = 90^\circ$ system, the PSD must be rotated so that the active region of the detector (long axis) is oriented in the PSD_2 direction. In contrast, for the $\phi = 0^\circ$ and 180° systems, the PSD is oriented so that the long axis of the PSD is in the PSD_1 direction. The above model can be used to simulate the trace made on the PSD by the reflected laser as the cantilever is made to deflect. Fig. 11a shows calculated data of the long axis (PSD_2 direction) versus the short axis

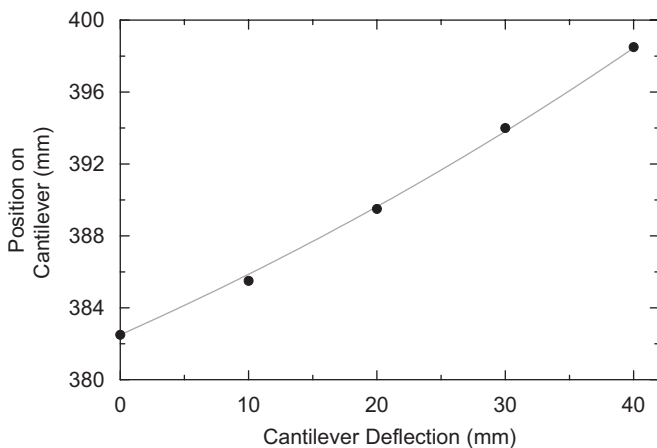


Fig. 7. Position of the laser spot on the cantilever versus cantilever deflection. Dots show experimental data taken with a macro-cantilever while the solid curve is calculated data from the model discussed within the text. In this data, the geometry of the macro cantilever was set to $\phi = 180^\circ$, $\theta = 69.9^\circ$, $D = 383.5 \text{ mm}$ and $\text{CL} = 410 \text{ mm}$.

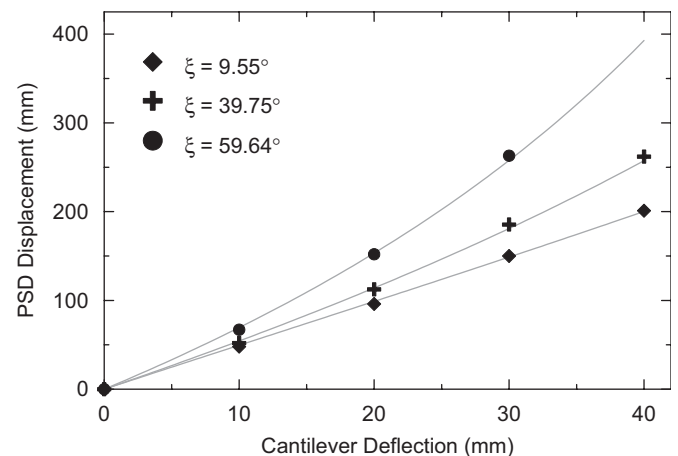


Fig. 8. Experimental (symbols) and calculated PSD displacement (solid curves) versus cantilever deflection for the following geometries: $\phi = 0^\circ$, $\theta = 69.9^\circ$, $L = 603.7 \text{ mm}$, $D = 383.5 \text{ mm}$, $\text{CL} = 410 \text{ mm}$ and $\xi = 9.55^\circ$, 39.75° and 59.64° .

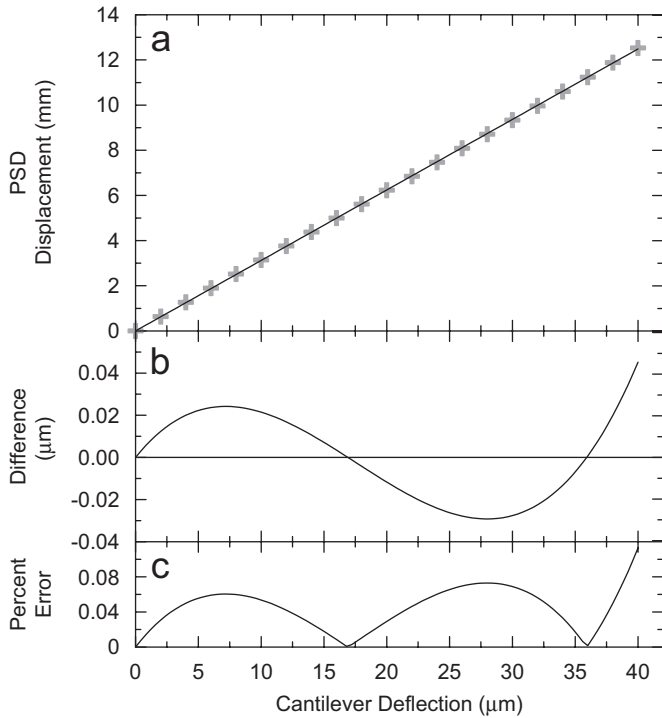


Fig. 9. (a) Calculated data (gray crosses) and linear fit (solid line) of PSD displacement versus cantilever deflection for the optimized geometry: $\phi = 0^\circ$, $\theta = 70^\circ$, $L = 3\text{ cm}$, $D = 325\ \mu\text{m}$, $CL = 350\ \mu\text{m}$ and an optimized PSD angle of $\xi = 13.88^\circ$. (b) Difference and (c) relative percent error between the calculated data and the linear fit shown in (a).

(-PSD₁ direction) of the PSD displacement (see Fig. 10) for the following geometries: $\phi = 90^\circ$, $\theta = 70^\circ$, $L = 3\text{ cm}$, $D = 325\ \mu\text{m}$, $CL = 350\ \mu\text{m}$ and $\xi = 10.0^\circ$, $\xi = 50.0^\circ$, $\xi = 60.0^\circ$, $\xi = 70.0^\circ$ and $\xi = 80.504^\circ$. For these calculations the cantilever was made to deflect as if subjected to an end moment to a maximum deflection of $40\ \mu\text{m}$. As shown, the curvature of the PSD trace increases with increasing values of ξ . The same results are obtained for calculations performed with a point load type deflection. However for the case of the point load, the curvature at the free end of the cantilever where the laser is made to reflect is much smaller than for end moment-type deflections. As a consequence the curving effects are slightly smaller.

The geometry described by system 2 has to date only been used in cantilever-based sensor instruments [21]. The PSD used in most cantilever sensors are only sensitive to the displacement of the reflected laser along the length (long axis) of the PSD. Therefore, provided the reflected laser spot remains within the active area of the PSD (approx. $10\ (\text{long}) \times 2\ (\text{wide})\ \text{mm}$) the measurement is unaffected by the curvature of the trace made by the reflected laser. Taking this under consideration it is possible to optimize the $\phi = 90^\circ$ system by linearizing the long-axis component of the trace made by the reflected laser versus the cantilever deflection. Fig. 11b shows the long-axis component of the PSD trace versus cantilever deflection of the same data shown in Fig. 11a. Although each curve is close to being linear, the optimized PSD angle

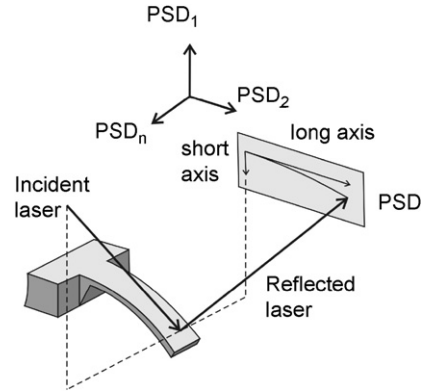


Fig. 10. Schematic representation showing the trace made on the PSD by the reflected laser for the $\phi = 90^\circ$ system. In this geometry the PSD must be rotated so that the active region of the PSD is along the PSD₂ direction.

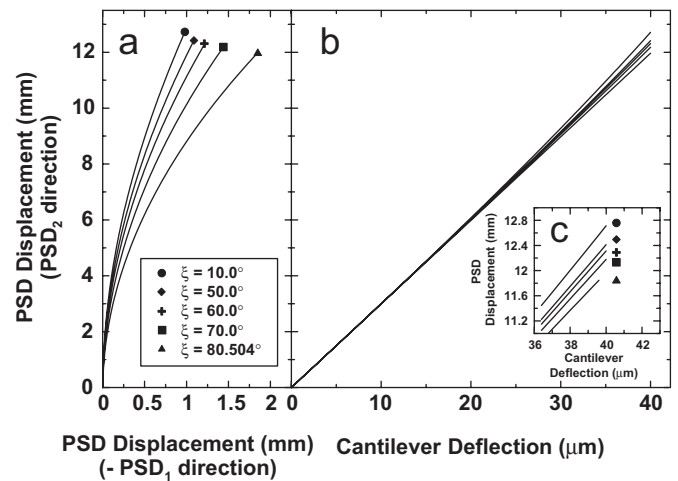


Fig. 11. (a) Calculated results showing the trace of the incident laser beam on the PSD during cantilever deflections for various PSD angles ξ for the following geometries: $\phi = 90^\circ$, $\theta = 70^\circ$, $L = 3\text{ cm}$, $D = 325\ \mu\text{m}$, $CL = 350\ \mu\text{m}$ and $\xi = 10.0^\circ$, 50.0° , 60.0° , 70.0° and 80.504° . (b) The long axis component (PSD₂ direction) of the laser beam trace on the PSD as a function of cantilever deflection for the same PSD angles shown in panel (a). (c) Expanded view of the PSD versus cantilever deflection curves shown in panel (b) with the associated PSD angles ξ .

is found to be 80.504° with a $\chi^2 = 7.23 \times 10^{-7}$. Fig. 11c shows the small differences between the five different curves shown in Fig. 11b. It is only at large cantilever deflections such as $40\ \mu\text{m}$ that the difference between the five curves is appreciable. In most cantilever-based experiments the cantilever is generally only made to deflect a few micrometers. For the case of a system with $\phi = 90^\circ$, $\theta = 70^\circ$, $L = 3\text{ cm}$, $D = 325\ \mu\text{m}$, $CL = 350\ \mu\text{m}$ with a cantilever subjected to a point load at $300\ \mu\text{m}$, the optimized PSD angle is $\xi = 81.04^\circ$ with $\chi^2 = 5.55 \times 10^{-7}$.

In order to further validate the above model, we show in Fig. 12 a comparison of the PSD displacement of both the short- and long-axis components versus cantilever deflection between experimental measurements (symbols) collected with a macro-cantilever and calculated data (solid curves) obtained from the model. The geometry of the

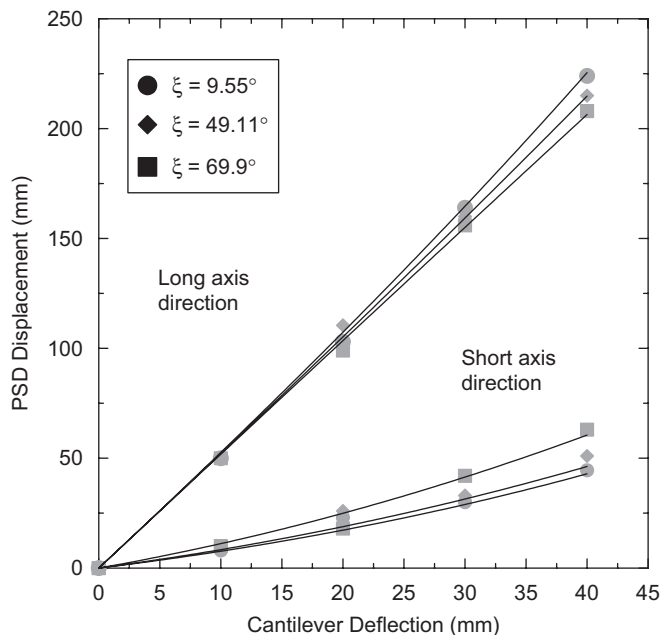


Fig. 12. Comparison between experimental measurements (symbols) collected with a macro-cantilever and calculated data (solid curves) obtained from the model described within the text. The geometry of the system was as follows: $\phi = 90^\circ$, $\theta = 69.9^\circ$, $L = 603.7$ mm, $D = 383.5$ mm, $CL = 410$ mm and $\xi = 9.55^\circ$, 49.11° and 69.9° .

system was as follows: $\phi = 90^\circ$, $\theta = 69.9^\circ$, $L = 603.7$ mm, $D = 383.5$ mm, $CL = 410$ mm and $\xi = 9.55^\circ$, 49.11° and 69.9° . As before, the agreement between the experimental data and our model is very good. In this case however, there is some noise in the experimental data, which originates from the inability to reduce torque effects on the macro-cantilever when forcing deflections.

In this paper, we have stressed the fact that for any kind of cantilever deflection and cantilever/laser beam detection system geometry it is possible to adjust the incident laser angle or the PSD angle such that the relationship between the PSD displacement and the cantilever deflection is nearly linear. It is sometimes desirable that this relationship not be linear but curved. For example, Figs. 4 a and b show how a PSD held at an angle $\xi = 0.0^\circ$ produces a concave curvature while a PSD held at an angle $\xi = 90.0^\circ$ produces a convex curvature. Clearly the concave curvature will provide more sensitive data at larger deflections while the convex curvature will provide more sensitive measurements at smaller cantilever deflections. This can be very useful when attempting to detect small deflection signal within a larger measurement range. Also due to system restrictions, it is not always possible to orient the incident laser angle or PSD angle in order to linearize the system. However as long as it is possible to obtain the values of D , L , CL , ϕ , θ , and ξ (for example, from manufacture specifications), the above model can be used to obtain the exact relationship between the cantilever deflection and PSD signal provided the proper cantilever curvature is taken into consideration. This last condition is not very stringent because end-

moment, point-load, and/or uniform load type deflections are induced by very different physical phenomena.

The above model has been incorporated into an excel spreadsheet and a visual basic program for end-moment and point load type deflections, respectively. We have also included a visual basic program to solve for x_{\max} in both Eqs. (5) and (9). This supporting material has been made available for download off our website at: http://www.physics.mun.ca/beaulieu_lab/papers/cantilever_analysis.htm. We welcome contact from users that would like to implement the above model into their instrument or as part of their data analysis.

5. Conclusion

We have shown by using elementary geometric optics and vector analysis that it is possible to completely characterize the cantilever/laser beam deflection system so as to obtain the exact relationship between the cantilever deflection and the PSD measurement. We have also shown that by adjusting either the incident laser angle or the PSD angle it is possible to tailor the relationship between the cantilever deflection and PSD displacement so as to make it more sensitive at different cantilever deflections or nearly linear to increase its ease of use. Elsewhere we have shown how the above model can be incorporated with new equipment design so as to obtain a self-calibrating system [16]. We believe that the analysis presented here and in Ref. [16] should be strongly considered when designing the next generation of cantilever-based sensor instruments or atomic force microscopes.

Acknowledgments

The authors would like to thank NSERC, CFI, IRIF, Memorial University, Genome Quebec, and McGill University for funding through various programs, grants and fellowships.

References

- [1] Gimzewshi, et al., Chem. Phys. Lett. 217 (1994) 598.
- [2] Davis, et al., J. Vac. Sci. Technol. B 18 (1996) 612.
- [3] Berger, et al., Science 276 (1997) 2021.
- [4] G. Meyer, N.M. Amer, Appl. Phys. Lett. 53 (24) (1988).
- [5] C.A.J. Putman, B.G. De Groot, N.F. Van Hulst, J. Greve, J. Appl. Phys. 72 (1) (1992).
- [6] C.A.J. Putman, B.G. de Groot, N.F. van Hulst, J. Greve, Ultramicroscopy (1992) 42.
- [7] A. Garcia-Valenzuela, J. Villatoro, J. Appl. Phys. 84 (1) (1998).
- [8] G. Moulard, G. Contoux, G. Gardet, G. Motyl, M. Courbon, Surf. Coat. Technol. 97 (1997).
- [9] T. Miyatani, M. Fujihira, J. Appl. Phys. 81 (11) (1997).
- [10] C. Kylvner, L. Mattsson, Rev. Sci. Instrum. 68 (1) (1997).
- [11] Z. Hu, T. Seeley, S. Kossek, T. Thundat, Rev. Sci. Instrum. 75 (2) (2004).
- [12] R. Raiteri, H.-J. Butt, M. Grattarola, Electrochim. Acta 46 (2000).
- [13] N.P. D'Costa, J.H. Hoh, Rev. Sci. Instrum. 66 (10) (1995).

- [14] G. Moulard, G. Contous, G. Motyl, G. Gardet, M. Courbon, *J. Vac. Sci. Technol. A* 16 (2) (1998).
- [15] S. Fujisawa, H. Ogiso, *Rev. Sci. Instrum.* 74 (12) (2003).
- [16] L.Y. Beaulieu, M. Godin, O. Laroche, V. Tabard-Cossa, P. Grütter, *Appl. Phys. Lett.* 88 (2006) 083108.
- [17] G.G. Stoney, *Proc. R. Soc. Lond. Ser. A* 82 (172) (1909).
- [18] R.W. Hoffman, *Physics of Thin Films* 3, Academic, New York, 1966, p. 211.
- [19] D. Sarid, *Scanning Force Microscopy: With Applications to Electric, Magnetic, and Atomic Forces*, Oxford University Press, January 1994.
- [20] G.E. Farin, D. Hansford, *The Geometry Toolbox for Graphics and Modeling*, Natick, Mass, 1998.
- [21] M. Godin, O. Laroche, V. Tabard-Cossa, L.Y. Beaulieu, P. Grütter, P.J. Williams, *Rev. Sci. Instrum.* 74 (2003) 4902.